A NARX network optimized with an adaptive weighted square-root cubature Kalman filter for the dynamic state of charge estimation of lithium-ion batteries.

TAKYI-ANINAKWA, P., WANG, S., ZHANG, H., XIAO, Y. and FERNANDEZ, C.

2023

A NARX network optimized with an adaptive weighted square-root cubature Kalman filter for the dynamic state of charge estimation of lithium-ion batteries

Paul Takyi-Aninakwa[a,*], **Shunli Wang**[a], **Hongying Zhang**[a], **Yang Xiao**[a], **Carlos Fernandez**[b]

[a] *School of Information Engineering, Southwest University of Science and Technology, Mianyang 621010, China*
[b] *School of Pharmacy and Life Sciences, Robert Gordon University, Aberdeen AB10-7GJ, UK*

ABSTRACT

Due to the high nonlinearities and unstable working conditions, accurately estimating the state of charge (SOC) by the battery management system (BMS) is a major challenge in ensuring the safety and reliability of lithium-ion batteries in electric vehicles. This paper presents a deep learning network, a nonlinear autoregressive model with exogenous inputs (NARX) network with a closed-loop architecture and transfer learning mechanism, which is optimized using a proposed adaptive weighted square-root cubature Kalman filter (AWSCKF) with a moving sliding window and an adaptive weighing coefficient for SOC estimation of lithium-ion batteries. The proposed AWSCKF method is established through square-root and cubature updates to optimize the statistical value of the state estimate, error covariance, and measurement noise covariance matrices, with the ability to incorporate high nonlinearities to filter out the noise, stabilize, and optimize the final SOC. To evaluate the effectiveness of the optimized NARX network and verify the proposed AWSCKF method, battery tests are carried out using a lithium cobalt oxide battery at various charge-discharge rates and a lithium nickel cobalt manganese oxide battery at temperatures of O and 45 °C under five complex working conditions. The SOC accuracy of lithium-ion batteries is enhanced by the hybrid method estimation process, which is based on sensitivity analysis and adaptation to various working conditions. The comprehensive results show that the proposed NARX-AWSCKF model achieves the overall best mean absolute error, root mean square error, and mean absolute percentage error values of 0.07293%, 0.0912%, and 0.40356%, respectively, under various complex conditions. By effectively utilizing battery domain knowledge for real-world BMS applications, the proposed model outperforms other existing methods in terms of high effectiveness, robustness, and potential to boost the NARX performance.

Keywords: State of charge; Lithium-ion battery; Nonlinear autoregressive model with exogenous inputs; Closed-loop architecture; Adaptive weighted square-root cubature Kalman filter

Nomenclature

ADAM	Adaptive moment estimate
AWSCKF	Adaptive weighted square-root cubature Kalman filter
BBDST	Beijing bus dynamic stress test
BMS	Battery management system
CALCE	Center for Advanced Life Cycle Engineering
CC-CV	Constant current-constant voltage
DL	Deep learning
TL	Transfer learning
DST	Dynamic stress test
EV	Electric vehicle
FUDS	Federal urban driving cycle
HL	Hidden layer
HPPC	Hybrid pulse power characterization
LM	Levenberg-Marquardt
LiC	Lithium cobalt oxide
LiNMC	Lithium nickel manganese cobalt
MAE	Mean absolute error
MAPE	Mean absolute percentage error
ME	Maximum error
ML	Machine learning
NARX	Nonlinear autoregressive model with exogenous inputs
OL	Output layer
RMSE	Root mean squared error
RT	Room temperature
SOC	State of charge
x_{max}	Maximum data value
	Nonlinear activation function
	Voltage residual covariance matrix
	Damping factor
x	Original input data
S	Lower triangular matrix
p	Posteriori error matrix
K	Kalman gain
Q	Process noise
R	Measurement noise
g	Forgetting factor
r	Weighing coefficient
a	Adaptive fading factor
	Adaptive weighing coefficient
γ	Moving sliding window size
L_w	Measurement noise
Q	Square-root factor of Q
S_Q	Square-root factor of R
S_R	Identity matrix
I	Time step
k	Nominal capacity
Q_n	Cubature point weight matrix
$\xi^{(i)}$	Actual SOC value
y	Estimated SOC value
$\hat{y}$	Estimated SOC error value
E	Total number of data samples
N	Normalized data value
x_{min}	Minimum data value
w	Network weight
b	Network bias
h	HL activation function
dx	Input delay coefficient
dy	Output delay coefficient

1. Introduction

Because global em1ss1ons from transportation have been nsmg steadily and now contribute to 27% of all carbon dioxide emissions, 70% of which come from internal combustion engine-powered vehicles, batteries are a key source of power for vehicles [1]. Electric vehicles (EVs) have been regarded as one of the potential alternatives that use renewable energy sources to minimize greenhouse gas emissions and global warming effects on the environment. The performance and effi- ciency of EVs have been substantially supported by lithium-ion batteries due to their appreciable advantages, such as low weight, high energy and power densities, low self-discharge rate, no memory effect, long cycle life, etc. [2-5].

The battery management system (BMS) is embedded to monitor the battery parameters, including current, voltage, etc., under various operating conditions, such as temperatures, current rates, etc., to accurately estimate the state of charge (SOC) to ensure the safety and reliability of the batteries in EVs [6,7]. SOC is the ratio of the remaining useful capacity during a given cycle to the maximum possible charge that can be stored in the battery (nominal capacity). The incidents involving EV fires show that continuous battery operation without explicit consideration of SOC may cause thermal runaways or even explosions. Besides the safety issues, the remaining drive range in EVs is estimated accurately, preventing unexpected system interruptions caused by overcharging, undercharging, and over-discharging, which can reduce the battery life or cause permanent damage to the battery [8]. However, due to the extreme nonlinear conditions encountered, it is highly challenging to measure an electrode's lithium content precisely; instead, the SOC is estimated from real-time measured current, voltage, temperature, etc. [9,10].

1.1. General classification of SOC estimation methods

In recent years, several methods have been proposed for the SOC estimation of lithium-ion batteries. These methods are divided into four categories: direct measurement based on parameter characterization, Coulomb counting, model-based, and data-driven methods [11-13]. However, several hybrid models have been proposed, which are a combination of one or more of the above-mentioned methods [14-16]. The direct measurement based on parameter characterization methods includes the electrochemical impedance spectroscopy (EIS) method [17] and the open-circuit voltage (OCV) [18] methods. The EIS evaluates the impedance properties of the battery across a broad frequency range. Although it has a simple implementation, its computation is sophisticated and extremely sensitive to the battery's status and operating conditions [19]. The OCV method estimates the SOC of the battery based on the OCV-SOC relationship because the active substance remaining in the electrodes and the electrochemical potentials are closely related, which is straightforward to implement. However, they are not suitable for onboard applications because they require a long resting time to reach equilibrium, which lasts for 2 h in some cases [20]. Otherwise, the internal capacitance may store some electricity, which leads to a false OCV measurement [21,22]. To overcome these issues, several algorithms and efforts have been proposed [21,23,24]. The Coulomb counting method is experimentally conducted by integrating the current flowing to and from the battery during the charge-discharge phases, which is easy to implement with low-power computational requirements [25]. However, it solely depends on the initial SOC value and suffers from a cumulative error due to drift and measurement errors of the current and uncertainties, such as noise, temperature, etc. [26,27].

For model-based estimation methods based on feedback correction, advanced Kalman filter (KF)-based methods are extensively proposed for SOC estimation, employing established battery models such as first- and second-order Thevenin and resistor-capacitor equivalent circuit models (ECMs) due to their simplicity and fidelity to monitor and simulate the dynamic responses of the battery mainly using current and voltage variables [28-31]. It regards the SOC as a hidden state and builds a state-space equation that maps the SOC to measured time-dependent variables like voltage and current [31,32]. However, because of variations in operating temperature, charge-discharge C-rates, voltage, etc., an inaccurate ECM coupled with the system's highly nonlinear characteristics tends to produce inaccurate estimates. Additionally, the voltage characteristics become incredibly challenging to calculate when the battery is exposed to complicated load profiles and unfavorable working conditions, leading to a computationally complex trial-and-error parameter identification procedure [33-35].

In recent years, data-driven methods have been the most effective at overcoming the shortcomings of other existing methods due to their superior self-adaptation, self-learning, and high estimation accuracy [36,37]. This method regards the lithium-ion battery as a "black box" rather than a mathematical estimation model. It directly maps the nonlinear relationship between the states and the measured variables such as current, voltage, temperatures, etc. [38,39]. They have been widely used for time-series predictions and have provided optimal performance in many research fields. The abilities of deep learning (DL) networks such as the recurrent neural network (RNN), long short-term memory (LSTM), the nonlinear autoregressive model with exogenous inputs (NARX), and other neural networks are well known because they can self-learn their weights and biases using gradient descent methods by the observation of the battery's electrochemistry [40-42].

1.2. Literature review

The NARX network has been used for estimating the state parameters of lithium-ion batteries because of its recurrent dynamic network with feedback mechanisms enclosing several layers. As a recurrent dynamic network with feedback mechanisms enclosing several layers, the NARX network has been utilized for estimating the state parameters oflithium- ion batteries. For instance, Wang et al. [43] proposed a NARX network for SOC estimation of lithium-ion batteries with a moving window method, which prevents the vanishing and explosion of the gradient at various ambient temperatures of 0, 25, and 45 °C under two working conditions. Herle et al. [44] proposed a NARX network for SOC esti- mation by verifying it under four working conditions at RT conditions using different hyperparameters. Guo et al. [45] established a NARX network and used a genetic algorithm to improve the accuracy of the estimated SOC using NASA battery #6. Also, as an improvement over the RNN to solve the gradient vanishing and explosion problems under long-term dependency conditions, the LSTM network has been exten- sively utilized for time-series SOC estimation due to its memory cell and gating mechanism during the backpropagation through time. Abbas et al. [46] studied the performance comparison of NARX and LSTM networks for SOC estimation at a temperature range of 5 to 25 °c. Under RT conditions, Wei et al. [47] proposed a hybrid NARX-LSTM network for SOC estimation and compared it to other existing SOC estimation methods under two working conditions. A hybrid PSO-LSTM network is proposed by Ren et al. [48] for SOC estimation, considering noise characterization under two different working conditions. By deter- mining the cause of unexpectedly inaccurate performances utilizing overexcited neurons under RT conditions, Xi et al. [49] developed a SOC estimation method employing a time-delayed RNN and LSTM network. Also, Bian et al. [50] proposed a computationally complex stacked bidirectional LSTM network for SOC estimation at temperatures of 0, 10, and 25 °C under two working conditions. Fasahat et al. [51] proposed a combined autoencoder and LSTM networks for SOC estimation of lithium-ion batteries under two working conditions and operating temperatures of 0, 25, and 45 °C. Yang et al. [52] estimated the SOC using an LSTM-RNN to model sophisticated battery behavior at tem- peratures ranging from 10 to 50 °c. The estimated SOC is noise filtered, and the estimation errors are reduced using the conventional UKF method.

In the era of big data usage and complex working conditions, the superior performance of these methods over existing SOC estimation methods needs to be quantitively demonstrated at different C-rates, temperatures, complex working conditions, battery chemistries, etc., to take full advantage of unseen data to realize accurate charged state estimation for real-world BMS applications, leveraging on the advantages of the recent development of transfer learning (TL) mechanisms to enhance the system's capacity and accuracy, since the thermodynamics, electrochemistry, and material constraints of the investigated battery technology are the underlying essential subjects [53,54].

1.3. Contributions of this paper

In this paper, a closed-loop NARX network with a TL mechanism is established to study its SOC estimation accuracy, robustness, and generalizability at different C-rates and temperatures under five complex working conditions. Then, an adaptive weighted square-root cubature Kalman filter (AWSCKF) method with a moving sliding window and an adaptive weighing coefficient is proposed through square-root and cubature updates to optimize the statistical value of the principal parameters for robust online BMS applications. The main contributions of this paper are highlighted below:

(1) The Levenberg-Marquardt (LM) method optimizes the NARX network and solves the gradient problems. Also, the adaptive moment estimation (ADAM) optimizer stabilizes the hyper-parameters to enhance the robustness of the network.
(2) The AWSCKF method adaptively filters out the noise, stabilizes, and optimizes the estimates, showing optimal SOC estimation results to function effectively for different batteries at various C-rates, temperatures, and working conditions.
(3) Because it is a data-driven initialization method, an accurate ECM or an OCV-SOC relationship mapping under various working conditions is not necessary for the proposed SOC estimation models.

1.4. Organization of the paper

The remaining sections of this paper are outlined as follows: Section 2 introduces the modeling mechanisms of the SOC estimation methods, the data augmentation processes, the overall framework, and the per- formance evaluation metrics. Section 3 describes the experimental battery and test characteristics. Section 4 is the results, discussions, and reviews. Section 5 is the conclusion of the paper and future work.

2. Modeling of the SOC estimation methods

2.1. The closed-loop NARX-based TL network for SOC estimation

In this paper, an optimized recurrent dynamic NARX network with feedback connections enclosing several layers is established. The closed-loop NARX network can deliver excellent SOC estimation solutions against noise and aging effects, but it needs proper adjustment of the hyperparameters, including hidden layer neurons and delay units in the input layer and output layer. The closed-loop design is employed because, rather than forming OLs using the HLs, it does so by employing limited feedback layers to increase the network's convergence speed and accuracy [56].

It consists of three layers: the input layer, HL, the feedback layer, and OL. Instead of using HLs, it forms OLs using limited feedback layers and outperforms conventional RNNs in terms of deep-learning ability, convergence speed, generalizability, and accuracy [55]. Its functional mathematical expression is presented in Eq. (1).

$$y(k) = f_o\left[y(k-1), y(k-2), \ldots, y\left(k-d_y\right), x(k), x(k-1), x(k-2), \ldots, x\left(k-d_x\right)\right] + e(k) \tag{1}$$

In Eq. (1), $f_o(\bullet)$ represents the nonlinear function of the OL and HL. $x(\bullet)$ and $y(\bullet)$ denote the input and output of the NARX network, respectively, at each discrete time step. d_x and d_y represent the input delay and output delay layers, respectively. y represents the output of the feedback delay layer, which is the SOC.

The model expression for the NARX network with three-dimensional inputs and a one-dimensional output is expressed in Eq. (2).

$$y(k) = f_o\left[b_o + \sum_{h=1}^{N} w_{h_o} \bullet f_h\left(b_h + \sum_{i_1=0}^{dx_1} w_{i_1|h} x_1(k-i_1) + \sum_{i_2=0}^{dx_2} w_{i_2|h} x_2(k-i_2) + \sum_{i_3=0}^{dx_3} w_{i_3|h} x_3(k-i_3) + \sum_{j=0}^{d_y} w_{jh} y(k-j)\right)\right] \tag{2}$$

In Eq. (2), $f_h(\bullet)$ represents the nonlinear functions of HL. i_i represents the information of the input delay layer, where i = 1, 2,3, ...,N. $w_{i_1}lh$, $w_{i_2}lh$, and $w_{i_3}lh$ represent the associated weights of the first input to the HL, the second input to the HL, third input to the HL, respectively. b_o and b_h are the biases of the OL and HL, respectively, which ensure flexibility and strengthen the network.

With activation functions, the perceptron uses tangent sigmoid (tansig) and pure linear (purelin) transfer functions at the **HL** and OL, respectively, with attached weights and biases. The tansig activation function used for the training of the network is mathematically expressed in Eq. (3).

$$f_o(x) = \frac{2}{1 + exp(-2x)} - 1 \tag{3}$$

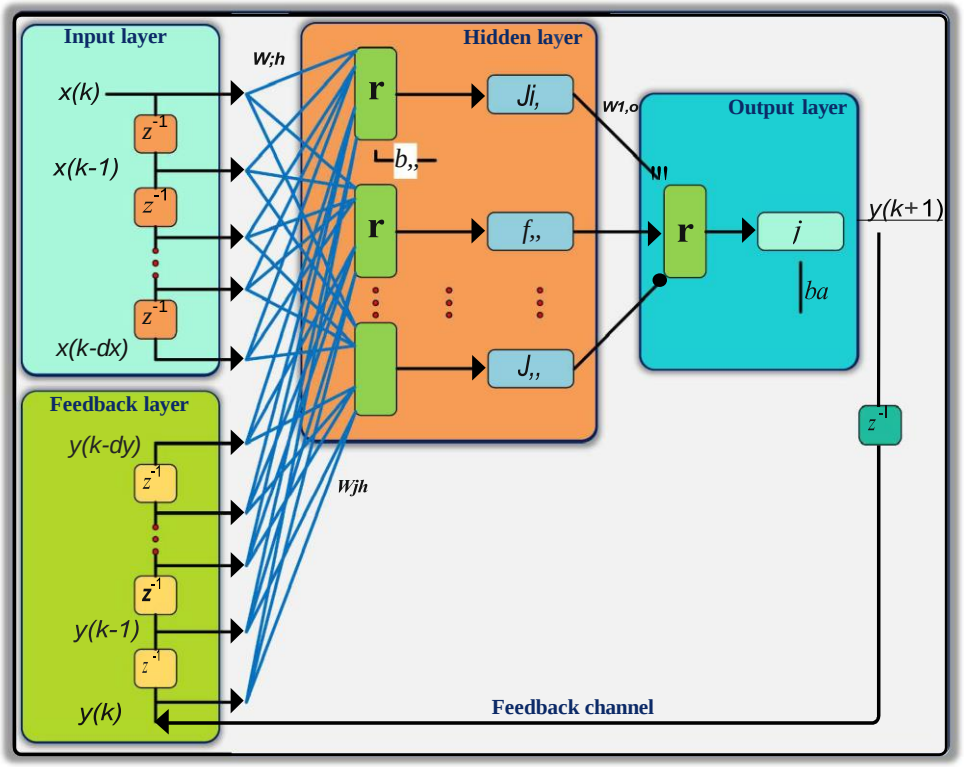

Fig. 1. The architecture of the established closed-loop NARX network.

The architecture of the established closed-loop NARX network is presented in Fig. 1.
The hyperparameter selection of the established closed-loop NARX is presented in Table 1.

Table 1
Hyperparameters selected for the network.

Hyperparameter	Unit
NARX layers (TL)	2
Fully connected layer	
Training goal	*10-B*
Training gradient	10-s
Epoch	250
Input delay	1:4
Feedback delay	1:4
HLs	15
Stochastic optimizer	ADAM
Training function	trainlm

The LM method is used to solve the occurrence of the gradient explosion and vanishing problems in the NARX network. It combines the gradient descent and Gauss-Newton methods by adaptively varying their updates. The gradient descent method lowers the sum of the squared errors by updating the damping factor along the steepest-descent direction. The total of the squared errors is decreased by the Gauss-Newton method by assuming that the least-squares function is locally quadratic for the parameters and locating the minimum of this quadratic. The calculation employs the second derivative approach, which substantially prevents the networks from entering the local optimum. The mathematical expression of the LM method that is used to adaptively update the hyperparameter is shown in Eq. (4).

$$x_k = x_{k-1} + \left[J_k^T J_k + \mu I\right]^{-1} J_k^T e_k \tag{4}$$

In Eq. (4), x_k and x_{k-1} represent the input vectors at different iteration time steps. J_k represents the Jacobian matrix, including the first derivatives of the network's errors with respect to the weights and biases. I is an identity matrix, e_k is the error of the network, *and* μ is the damping factor used to tune the accuracy convergence speed.

If the decrease is rapid or *f (x)* falls below the current number of iterations, a smaller value is used to bring it closer using the Gauss- Newton method by allowing μ = μ/y. Conversely, if the decrease is slow or *f(x)* increases above the current iterations, a larger μ value is used to make it closer using the gradient descent method by letting μ = /Ix y, where r is a constant greater than 1. The LM method offers good stability, quick convergence, and solves the gradient problems of the NARX network for accurate SOC estimation of the battery.

2.2. Training procedure for the optimized NARX network

The general training procedures for the established methods are dis- cussed in detail in this section, including the stochastic optimizer and training loss functions used to study the training and testing abilities of each network. The stochastic optimizer plays a significant role in the search for the converging point during the training of the NARX network. Using the right optimizer gives the network superior performance. The ADAM optimizer is then used to stabilize the hyperparameters. It ensures faster optimization of the hyperparameters of the NARX network by effectively updating their weights and biases.

The optimized NARX network is trained using a mini-batch size based on each network's adaptability and the amount of available hardware memory to ensure an estimation with reduced noise and optimal accuracy and efficiency. The common solutions are usually to retrain the network with more or fewer layers and neurons and add a dropout layer with a certain dropout probability to prevent overfitting.

Such an overall trial-and-error process makes neural networks less attractive for battery state estimation, especially when the results are also difficult to explain. Therefore, the TL mechanism structure of the closed-loop NARX network is established, as presented in Section 2.3.

The RMSE is used as a loss function to study the training and testing performance of the network. Its mathematical expression is presented in Eq. (5).

$$Loss\ function = \sqrt{\frac{1}{N}\sum_{k=1}^{N}(y_k - \hat{y}_k)^2} \tag{5}$$

In Eq. (5), N is the total number of data samples, y_k is the actual SOC, and $\hat{y}_k$ is the estimated SOC by the established models at time step k.

The training and testing of the NARX network and SOC optimizations are carried out using MATLAB 2021 on an Intel(R) Core (TM) i5- 7300HQ computer with a CPU speed of 2.50 GHz.

2.3. The transfer learning mechanism

Lithium-ion batteries in EVs have their unique characteristics because they vary from manufacturer to manufacturer. The purpose is to establish a method based on neural networks that is versatile and can better adapt to different lithium-ion battery chemistries. To effectively apply DL methods to various EV applications, the employment of the TL mechanism can maximize efficiency with limited resources. With the aid of hyperparameters, features, working conditions, etc., the recent development of TL offers a novel direction for enhancing a system's capacity to recognize and apply the knowledge learned in earlier do- mains to new domains [56]. Using a TL mechanism, data-driven methods can be initially taught using a limited dataset obtained from various experimental tests. Then, after being implemented on an EV, the network can be retrained using actual data gathered during its operation cycles by transferring the knowledge gained from the known data to the unseen data as the source and target layers, respectively [35]. It functions as a type of network architecture and aids in monitoring the changes in the SOC trends of the battery as it ages to enhance the generalization learning ability and estimation accuracy, as well as improve the nonlinear fitting ability of the conventional NARX network by optimizing its structure during the implementation [41]. It can drastically reduce training time and computational resources by retraining all the layers or by freezing some layers while retraining others to speed up the development of the new layer and improve the accuracy of the retrained layers [57]. As a result, a pre-trained network can be modified with a new dataset to improve parts of its layers, out- performing the creation of a brand-new NARX network from scratch. In this context, it is possible to use the pre-trained network for different battery datasets at various charge-discharge rates and temperatures to estimate both the short- and long-term SOC. It is important to note that the results are independent because the NARX network directly maps the input current and voltage sequence to estimate the SOC. Therefore, an initial SOC value is not required for the estimations.

2.4. Data description and pre-processing

Since data pre-processing is significant for accurate SOC estimation, the associated current, voltage, and temperature $[I_k, V_k, T_k]$ variables are measured based on real-time working conditions at an interval of 0.1 s, which are retrieved and normalized to improve the quality of the input data using the min-max normalization method. The original data for each feature sequence is normalized in the range [-1, 1] before training and testing to optimize the robustness, convergence rate, and speed up the gradient descent of the NARX network, as presented in Eq. (6).

$$x_n = \frac{2(x - x_{min})}{x_{max} - x_{min}} - 1 \tag{6}$$

In Eq. (6), x_n and x are the normalized and original data values at each time step, respectively. x_{min} and x_{max} are the minimum and maximum values in the dataset, respectively.

Even though the NARX network and its hyperparameters are optimized, however, the results are affected by the nonlinearities that occur when the battery is operating under different C-rates, temperatures, and complex working conditions. Therefore, the proposed AWSCKF method is discussed in Section 2.5.

2.5. AWSCKF-based optimization method

Based on the state-space model of nonlinear systems with zero mean Gaussian white noise, the CKF can achieve the best estimates of the battery's state parameters by applying partial derivative and first-order Taylor series expansion, which has been utilized effectively in many research fields [26,58].

The Cholesky decomposition requires matrices to be symmetric positive (semi) definiteness. The matrix symmetry must be positive definiteness for the Cholesky decomposition to function. However, due to rounding and discretization-related numerical calculation errors, the noise covariance matrices of the ACKF method might not remain sym- metric positive definite throughout the iteration, which could result in filter divergence [59]. Therefore, the proposed AWSCKF method with an adaptive sliding update for the process and measurement noise covariance matrices, in addition to the state estimate and error covariance matrix, includes innovative updates to increase the method's accuracy. Furthermore, the proposed method optimally exponentiates the Kalman gain to weigh the amount of the innovation residual during the poste- riori state estimate to optimize the numerical accuracy and filtering stability.

The recursive working steps of the proposed AWSCKF method begin with state variable initialization, as presented in Eq. (7).

$$\begin{cases} \widehat{x}_0 = E[x_0] \\ S_0 = \sqrt{P_0} \end{cases} \tag{7}$$

In Eq. (7), S_0 is a square-root factor of the error covariance matrix P_0. Time update:

The first factorization and decompose of the priori error covariance matrix is shown in Eq. (8).

$$\begin{cases} S_{k-1|k-1} = Chol(P_{k-1|k-1}) \\ P_{k-1|k-1} = S_{k-1} S_{k-1}^T \end{cases} \tag{8}$$

To propagate them through the state transition function, the cubature point is determined, as shown in Eq. (9).

$$\begin{cases} x_{k-1|k-1}^{(i)} = \widehat{x}_{k-1|k-1} + S_{k-1|k-1}\xi^{(i)}, i = 1, 2, \ldots, m \\ x_{k|k-1}^{(i)*} = f\left(x_{k-1|k-1}^{(i)}\right) \end{cases} \tag{9}$$

In Eq. (9), $x^{(i)}_{k\text{-}1/k\text{-}1}$ is the cubature point, $m = 2N$ is the total number of cubature points, N is the dimension of the state input vectors, $\xi^{(i)}$ is the weight matrix of the cubature point, which consists of n-dimensional unit matrix, as shown in Eq. (10).

$$\begin{gathered} \xi^{(i)} = \begin{cases} \sqrt{N[1]^{(i)}}, i = 1, 2, \ldots, m \\ -\sqrt{N[1]^{(i)}}, i = N+1, N+2, \ldots, m \end{cases} \\ [1]^{(i)} = \left[\begin{pmatrix} 1 \\ 0 \\ \vdots \\ 0 \end{pmatrix} \cdots \begin{pmatrix} 0 \\ 0 \\ \vdots \\ 1 \end{pmatrix} \begin{pmatrix} -1 \\ 0 \\ \vdots \\ 0 \end{pmatrix} \cdots \begin{pmatrix} 0 \\ 0 \\ \vdots \\ -1 \end{pmatrix} \right] \end{gathered} \tag{10}$$

In Eq. (10), [1] is the identity matrix, and i denotes the ith column vector. The mean value of the state estimate and the square-root factor of the error covariance matrix is calculated, as shown in Eq. (11).

$$\begin{cases} x_{k|k-1} = \dfrac{1}{m} \displaystyle\sum_{i=1}^{2N} \widehat{x}_{k-1}^{(i)} \\ S_{k|k-1} = Tria\left(\left[x_{k|k-1}^{(i)*}, S_{Q|k-1}\right]\right) \end{cases} \tag{11}$$

In Eq. (11), $S_{Q/k-1}$ denotes the square-root factor of the process noise covariance matrix Q_{ak-1}. The weighted central matrix $x^{(I)*}_{k/k-1}$ is expressed, as shown in Eq. (12).

$$x_{k|k-1}^{(i)*} = \frac{1}{\sqrt{m}}\left[x_{k|k-1}^{1*} - \widehat{x}_{k|k-1}, x_{k|k-1}^{2*} - \widehat{x}_{k|k-1}, x_{k|k-1}^{3*} - \widehat{x}_{k|k-1}, \ldots, x_{k|k-1}^{m*} - \widehat{x}_{k|k-1}\right] \tag{12}$$

In Eq. (12), the operation of $Tria(\bullet)$ is defined as follows: let R be the upper triangular matrix of the QR decomposition of the matrix A^T. The QR decomposition of the state transition matrix A is expressed, as shown in Eq. (13).

$$S = Tria(A) = R^T \tag{13}$$

In Eq. (13), S is the lower triangular matrix. Measurement update:

The cubature point is updated and propagated through the measurement function, as shown in Eq. (14).

$$\begin{cases} x_{k|k-1}^{(i)} = \widehat{x}_{k|k-1} + S_{k|k-1}\xi^{(i)} \\ z_{k|k-1}^{(i)} = h\left(x_{k|k-1}^{(i)}\right) \end{cases} \tag{14}$$

The mean value of the measurement estimate is calculated and the square-root factor of the posteriori error covariance matrix, as shown in Eq. (15).

$$\begin{cases} \widehat{z}_{k|k-1} = \dfrac{1}{m}\sum_{i=1}^{m} z_{k|k-1}^{(i)} \\ S_{k|k-1}^{zz} = Tria([Z_{k|k-1}, S_{R|k}]) \end{cases} \tag{15}$$

In Eq. (15), S_{Rlk} denotes the square-root factor of measurement noise covariance matrix R_k. Then, the weighted central matrix Z_{klk-1} is calculated, as shown in Eq. (16).

$$Z_{k|k-1} = \frac{1}{\sqrt{m}}\left[z_{k|k-1}^{1} - \widehat{z}_{k|k-1}, z_{k|k-1}^{2} - \widehat{z}_{k|k-1}, z_{k|k-1}^{3} - \widehat{z}_{k|k-1}, \ldots, z_{k|k-1}^{m} - \widehat{z}_{k|k-1}\right] \tag{16}$$

The measurement innovation covariance matrix is calculated and the cross-covariance matrix between state and measurement is shown in Eq. (17).

$$\begin{cases} P_{k|k-1}^{zz} = S_{k|k-1}^{zz}\left(S_{k|k-1}^{zz}\right)^{T} \\ P_{k|k-1}^{xz} = X_{k|k-1}Z_{k|k-1}^{T} \end{cases} \tag{17}$$

Then, the weighted central matrix X_{klk-l} and Kalman gain is obtained, as shown in Eq. (18).

$$\begin{cases} X_{k|k-1} = \dfrac{1}{\sqrt{m}}\left[x_{k|k-1}^{1} - \widehat{x}_{k|k-1}, x_{k|k-1}^{2} - \widehat{x}_{k|k-1}, x_{k|k-1}^{3} - \widehat{x}_{k|k-1}, \ldots, x_{k|k-1}^{m} - \widehat{x}_{k|k-1}\right] \\ K_k = P_{k|k-1}^{xz}\left(P_{k|k-1}^{zz}\right)^{-1} \end{cases} \tag{18}$$

The state estimate is updated and the corresponding square-root factor of the error covariance matrix, as shown in Eq. (19).

$$\begin{cases} \widehat{x}_{k|k} = \widehat{x}_{k|k-1} + K_k^{\gamma}(z_k - \widehat{z}_{k|k-1}) \\ S_{k|k} = Tria\left(\left[X_{k|k-1} - K_k Z_{k|k-1}, K_k S_{R,k}\right]\right) \end{cases} \tag{19}$$

In Eq. (19), y is an adaptive weighing coefficient for the Kalman gain, which is adjusted as $1 \le \gamma \le 4$. It is introduced to enhance the gain's value to be added to the residual during the posteriori state estimation. The adaptive update of process and measurement noise covariance matrices are shown in Eq. (20).

$$\begin{cases} Q_k = K_k H_k K_k^{T} + e_k \\ R_k = H_k + \sum_{i=0}^{2N} W_N^{(i)}\left(\widehat{y}_{k|k-1}^{(i)} - y_k\right)\left(\widehat{y}_{k|k-1}^{(i)} - y_k\right)^{T} \\ H_k = \sum_{i=k-L_w+1}^{k} e_k e_k^{T}, L_w = 1, 2, \ldots, 5 \end{cases} \tag{20}$$

In Eq. (20), H_k is the approximate estimate of the voltage residual covariance matrix, and L_w is the moving sliding window size that matches the covariance matrices.

In this paper, the A and B are the state-transition matrix and control-input matrix, which are applied to the state estimate x_{k-1} and control-input vector u_k, respectively. C_k is the measurement matrix at time step k, which maps the state space into the measured space. All these variables are initialized as 1. As a result, the AWSCKF method with a moving sliding window and the adaptive weighing coefficient is adaptable enough to deal with uncertainties and noise updates using the optimized square root, cubature, and exponential Kalman gain updates for accurate and reliable SOC estimation.

As one of the critical functions of the BMS, the mathematical expression for the SOC is presented in Eq. (21).

$$SOC_k = SOC_0 - \frac{1}{Q_n}\int_0^{N} \eta I_k dk \tag{21}$$

In Eq. (21), SOC_k is the SOC estimated value at time step k, and SOC_0 is the SOC value at time step 0. η is the Coulombic efficiency, which is defined as 1, I_k is the working current at time step k, and Q_n is the nominal capacity of the battery.

2.6. *Architectural framework for the SOC performance study*

The entire framework, which includes the dynamic working conditions, characteristic datasets, experimental platform, data preprocessing, the comparative study NARX network, NARX-AWSCKF model, and other existing methods, etc., are presented in Fig. 2.

2.7. *Performance evaluation metrics*

In this paper, to critically evaluate the feasibility and validity of the NARX network and the AWSCKF-based optimization method for SOC estimation, the maximum error (ME), mean absolute error (MAE), root mean square error (RMSE), and mean absolute percentage error (MAPE) metrics are employed, as presented in Eq. (22).

$$\begin{cases} E_k = y_k - \hat{y}_k \\ ME = max1, 2, \ldots, N|E_k| \\ MAE = \dfrac{1}{N}\sum_{k=1}^{N}|E_k| \\ RMSE = \sqrt{\dfrac{1}{N}\sum_{k=1}^{N}(E_k)^2} \\ MAPE = \dfrac{100\%}{N}\sum_{k=1}^{N}\left|\dfrac{E_k}{y_k}\right| \end{cases} \tag{22}$$

In Eq. (22), N is the total number of steps in the data sample, and E_k is the estimated SOC error at time step k. Y_k is the actual SOC and $\hat{y}_k$ is the SOC estimated at time step k.

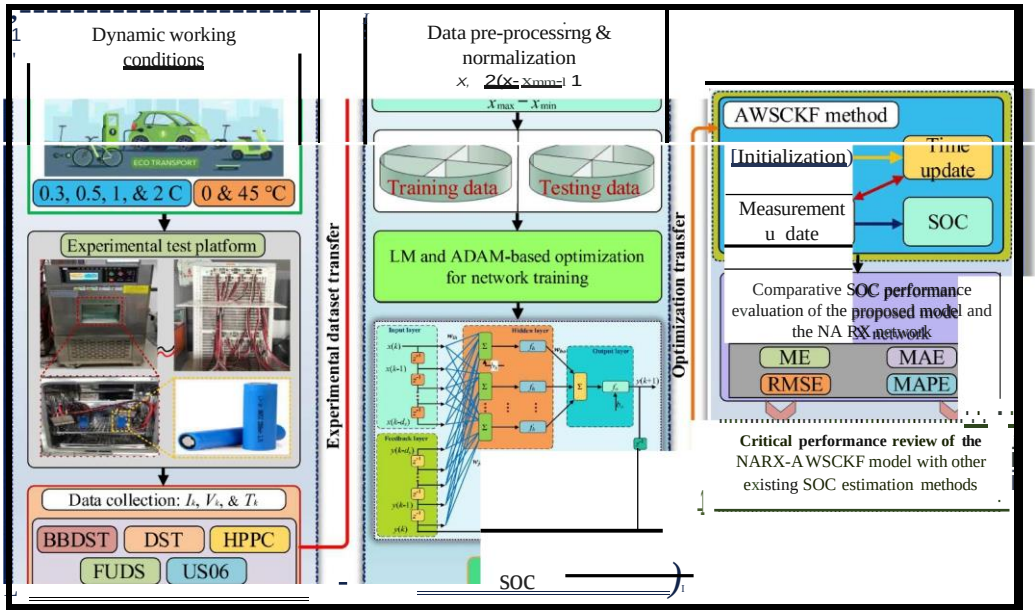

Fig. 2. The flowchart for the SOC performance study and review of the models.

3. Experimental batteries and tests characteristics

In this paper, battery tests are carried out on an ICR18650-26 V (Lithium Cobalt Oxide, LiC) battery at different C-rates under the Beijing bus dynamic stress test (BBDST), hybrid pulse power characterization (HPPC), and dynamic stress test (DST) working conditions at RT con- ditions (28~32 °C). Then, the datasets from the CALCE repository for an INR18650-20R (Lithium Nickel Manganese Cobalt Oxide, LiNMC) battery under the BBDST, the federal urban driving schedule (FUDS), and US06 working conditions at temperatures of O and 45 °C are employed to test and verify the performance of the proposed AWSCKF method. The technical specifications of the LiC and LiNMC batteries are presented in Table 2.

Table 2
Technical specifications of the experimental batteries.

Parameter		Lie battery	LiNMC battery
Nominal capacity		2.55 Ah	2.00 Ah
Nominal voltage		3.60 V	3.60 V
Charging	Cut-off voltage	4.20 ± 0.05 V	4.20 ±0.05 V
	Standard	0.5 C	0.5 C
Discharging	Cut-off voltage	2.5 ± 0.05 V	2.5 ±0.05 V
	Standard	0.5 C	0.25 C
LiC:	Higher specific energy density but a higher internal resistance.		
LiNMC:	Hybrid chemistry for increased capacity with reduced cost and internal resistance. [60,61]		

For the different C-rate battery tests using the LiC battery, a Neware battery test equipment (CT-4016) with a ±0.1% full-scale accuracy is used. It has a maximum current of 100 A, a range of charge-discharge voltage of 0.025- 5 V, and a maximum power of 14 kW. The current, voltage, capacity, energy, etc. datasets are retrieved in real-time via the peripheral data acquisition cable (TCP/IP) interconnecting the host computer and battery test equipment.

All the battery tests begin with the constant current/constant voltage (CC/CV) charging method, which is applied until the maximum capacity is reached. A 30-minute rest is followed to ensure thermal and electro- chemical equilibrium, after which the discharge steps continue. The characteristics of the varying charge-discharge rate current and voltage under the BBDST, DST, and HPPC working conditions at RT are pre- sented in Fig. 3.

For the temperature study using a cylindrical LiNMC battery, the open-access datasets from the CALCE repository are obtained by applying various drive cycles with standard charge-discharge profiles. Initially, the battery is subjected to a CC/CV charging profile. All tests are performed at temperatures of 0, 25, and 45 °C in tandem under the BBDST, FUDS, and US06 working conditions, which are standard tests to confirm battery SOC estimation under dynamic conditions. They simu- late the operation of an EV in an urban environment. During the dis- charging phase, the battery's instantaneous voltage and current values are logged at a sampling frequency of 1 Hz. In the paper, the BJDST is defined as the BBDST working condition. However, the temperature datasets used are 0 and 45 °C because the charge-discharge rate tests are conducted at RT conditions. More information about the test procedure and the characteristic current and voltage profiles at different temperatures can be obtained in [49,62,63].

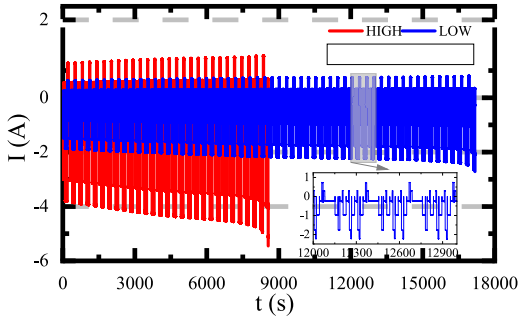

(i) Current variation for low and high-power rates under the BBDST working condition

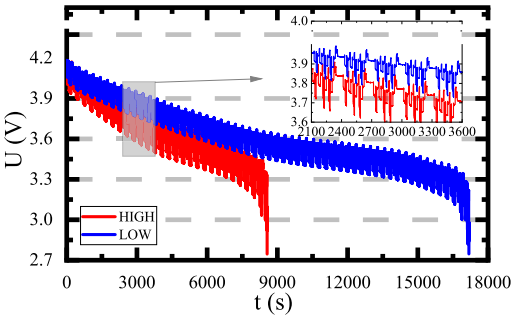

(ii) Voltage variation for low and high-power rates under the BBDST working condition

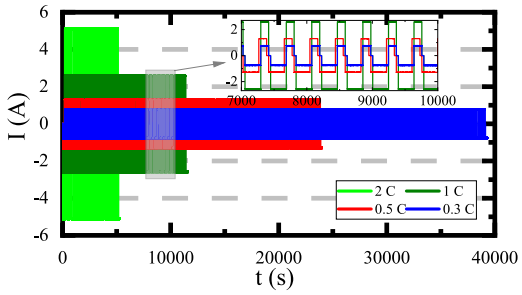

(i) Current variation for 0.3, 0.5, 1, and 2 C under the DST working condition

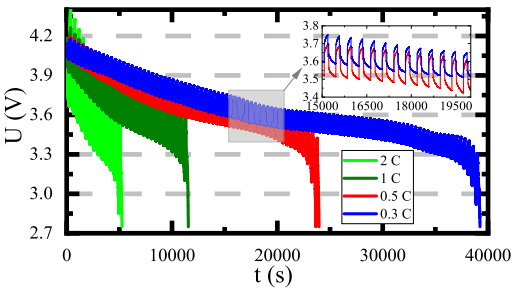

(ii) Voltage variation for 0.3, 0.5, 1, and 2 C under the DST working condition

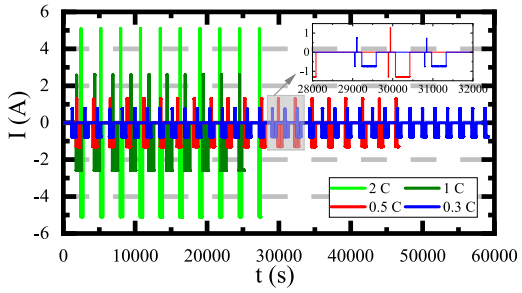

(i) Current variation for 0.3, 0.5, 1, and 2 C under the HPPC working condition

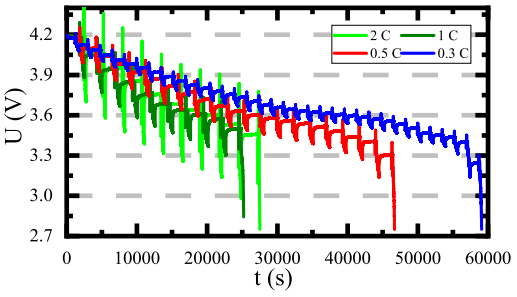

(ii) Voltage variation for 0.3, 0.5, 1, and 2 C under the HPPC working condition

Fig. 3. Current and voltage curves for different charge-discharge rates under the BBDST, DST, and HPPC working conditions.

4. Results and discussion

In this paper, to test the deep learning, generalization, and transfer learning abilities of the NARX network, the charge-discharge rate datasets for 2 C under the DST and HPPC working conditions are interchangeably selected as training for SOC estimation. In addition, due to the small sample dimensional characteristics and the number of iterations required to ensure computational efficiency and high accuracy, 0 °C temperature datasets under the FUDS and US06 working conditions are interchangeably selected as the training dataset for the NARX network in such a way that generalization and transfer learning abilities are exhibited. Meanwhile, the remaining unseen datasets are used for charge-discharge rate and temperature SOC testing and validation under various working conditions.

4.1. Comparative SOC estimation pe,jormance of the optimized NARX and NARX-AWSCKF models

This section presents the comparative SOC estimation results of the optimized NARX network and the proposed NARX-AWSCKF model at different C-rates and temperatures. In this paper, the process noise (Q), measurement noise (R), and initial value for the error covariance matrix (P_0) is set as 10^{-6}, $2*10^{-2}$, and 10^{3}, respectively, using the same moving sliding window sizes.

4.1.1. SOC estimation at different charge-discharge rates

The comparative SOC results of the optimized NARX and proposed NARX-AWSCKF models at different charge-discharge rates under the BBDST, DST, and HPPC working conditions are conducted. The SOC estimation results under the BBDST working condition are presented in Fig. 4.

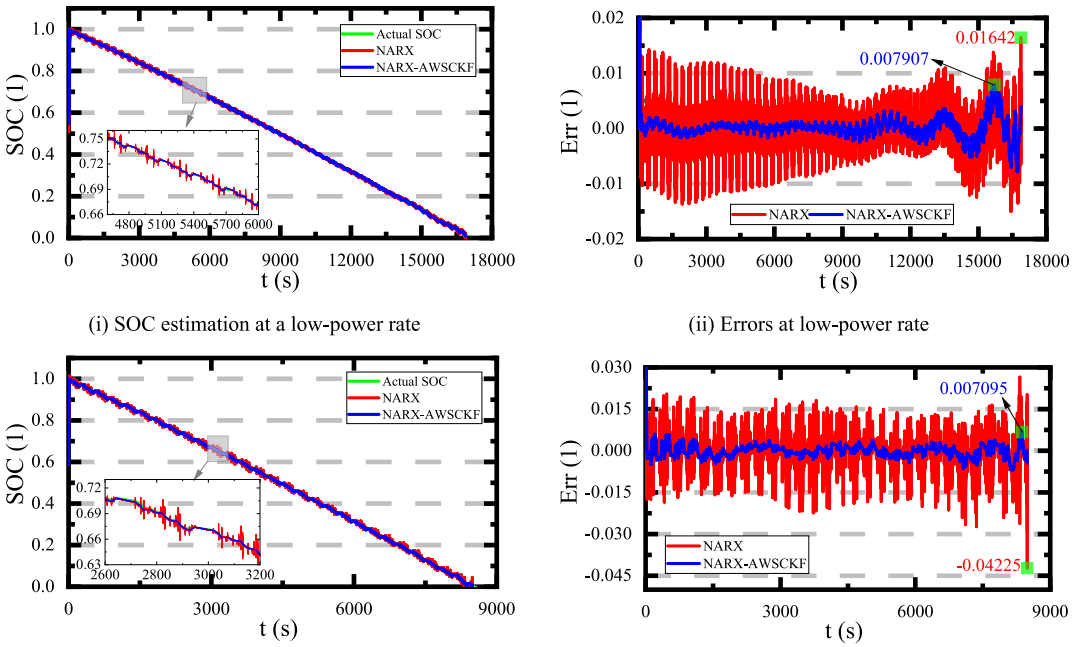

(i) SOC estimation at a low-power rate (ii) Errors at low-power rate

(i) SOC estimation at high-power rate (ii) Errors at high-power rate

Fig. 4. Comparative SOC estimation results of the NARX and NARX-AWSCKF models at different charge-discharge rates under the BBDST working condition.

In Fig. 4, it can be observed that the estimations by the NARX network have more noise compared to the proposed NARX-AWSCKF model at high and low-power rates. Using a low power rate, the NARX network has an ME value of 1.642%, while the proposed NARX-AWSCKF model has an ME value of 0.7907%, which represents a performance improvement of 51.85%. Also, at a high-power rate, the NARX network estimates the SOC with an ME value of 4.225%, while the proposed NARX-AWSCKF model has an ME value of 0.7095%, representing a performance improvement of 83.20%. At both power rates, it can be observed that the levels of noise are the same when using the NARX network. However, the noise is more concentrated at a high power rate compared to a low power rate. Meanwhile, the proposed NARX- AWSCKF model ensures the reduction of noise for optimized and accurate SOC estimation performance.

The comparative SOC performance for the NARX and NARX- AWSCKF models at 0.3, 0.5, 1, and 2 C-rates are conducted under the DST working condition, as presented in Fig. 5.

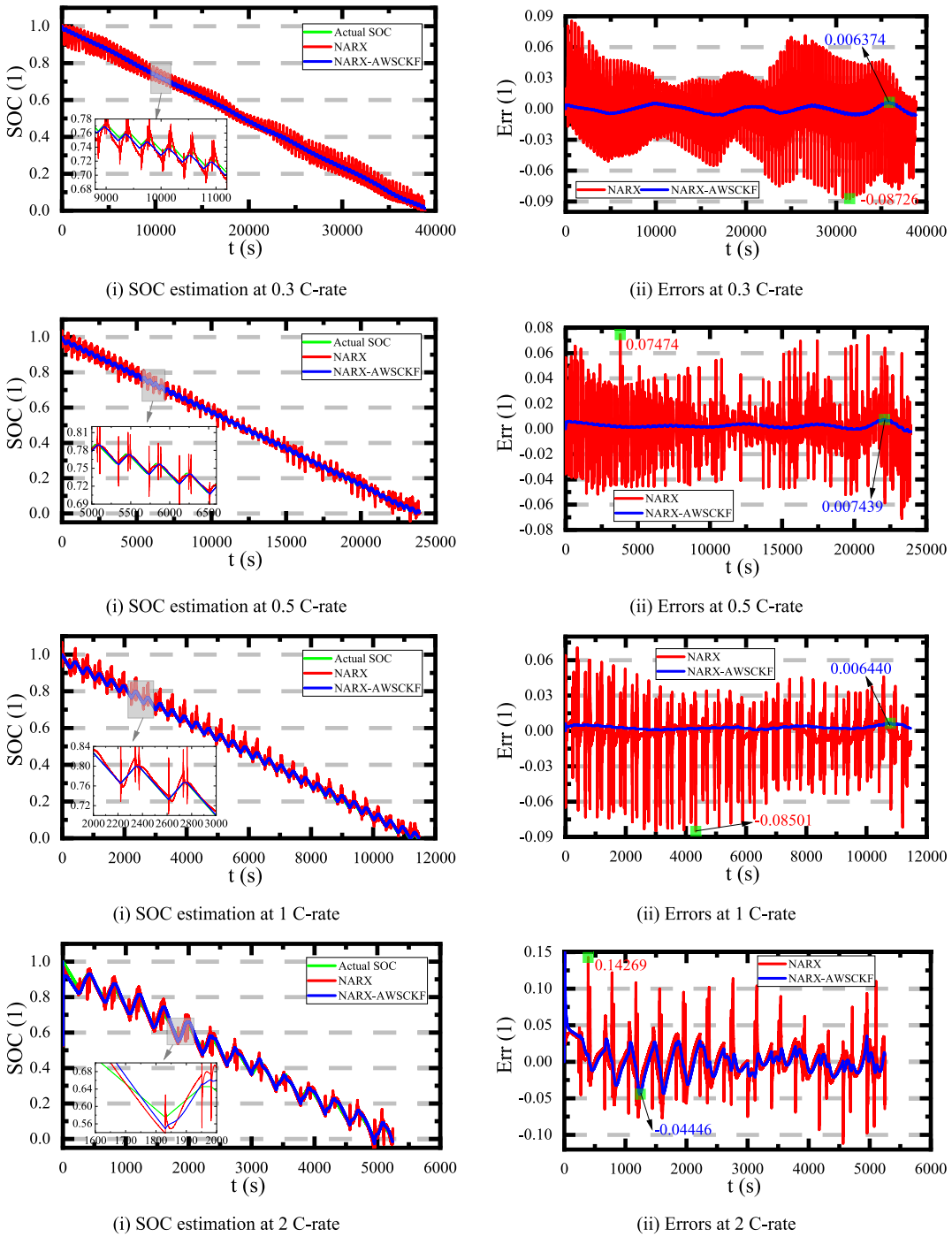

(i) SOC estimation at 0.3 C-rate

(ii) Errors at 0.3 C-rate

(i) SOC estimation at 0.5 C-rate

(ii) Errors at 0.5 C-rate

(i) SOC estimation at 1 C-rate

(ii) Errors at 1 C-rate

(i) SOC estimation at 2 C-rate

(ii) Errors at 2 C-rate

Fig. 5. Comparative SOC estimation results of the NARX and NARX-AWSCKF models at different charge-discharge rates under the DST working condition.

In Fig. 5, it can be observed that the estimations of the NARX network are highly affected by noise, showing high error spikes and noise at 2C and a concentrated noise increasing with decreasing C-rates. For the SOC estimation results at 0.3, 0.5, 1, and 2 C-rates, the NARX network has ME values of 8.726%, 7.474%, 8.501%, and 14.269%, respectively.

Meanwhile, the NARX-AWSCKF model has stable SOC estimates and ME values of 0.6374%, 0.7439%, 0.6440%, and 4.446% at 0.3, 0.5, 1, and 2 C-rates, respectively. These results respectively represent a performance improvement of 92.70%, 90.05%, 92.42%, and 68.84%, which are significant optimization values for practical BMS applications. Furthermore, the proposed NARX-AWSCKF model has more consistent and optimal performance with less noise and fluctuations at different C- rates.

Furthermore, the comparative SOC performance for the NARX and NARX-AWSCKF models at 0.3, 0.5, 1, and 2 C-rates are conducted under the HPPC working condition are presented in Fig. 6.

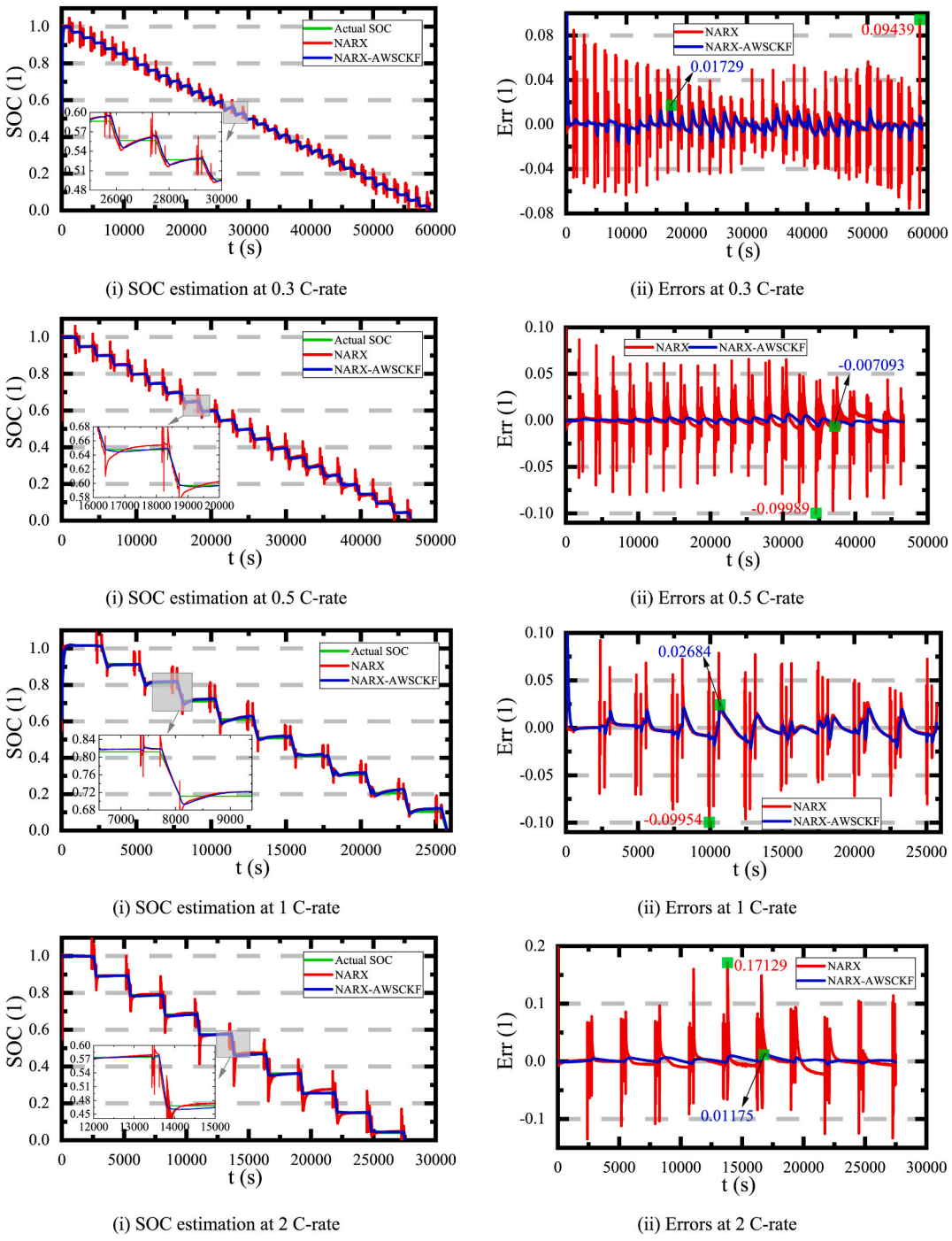

(i) SOC estimation at 0.3 C-rate

(ii) Errors at 0.3 C-rate

(i) SOC estimation at 0.5 C-rate

(ii) Errors at 0.5 C-rate

(i) SOC estimation at 1 C-rate

(ii) Errors at 1 C-rate

(i) SOC estimation at 2 C-rate

(ii) Errors at 2 C-rate

Fig. 6. Comparative SOC estimation results of the NARX and NARX-AWSCKF models at different charge-discharge rates under the HPPC working condition.

Fig. 6 shows that the SOC estimations of the NARX network have more noise even at low C-rates, which peak at 2 C, which are similar to the estimations under the DST working condition. For the results, the optimized NARX network estimates the SOC with ME values of 9.439%, 9.9989%, 9.954%, and 17.129%, at 0.3, 0.5, 1, and 2 C-rates, respectively, with high noise effects. Meanwhile, after optimization, it can be observed that the proposed NARX-AWSCKF model estimates the SOC with ME values of 1.729%, 0.7093%, 2.684%, and 1.175%, respectively, in the same C-rate order, which represent a performance improvement of 81.68%, 92.90%, 73.04%, and 93.14%.

Generally, it can be observed that the proposed NARX-AWSCKF model has optimal performance compared to the NARX network at different C-rates under the BBDST, DST, and HPPC working conditions, showing consistent optimization performance.

4.1.2. Pe,jonnance evaluation at different charge-discharge rates

The MAE, RMSE, and MAPE metrics are used to critically evaluate the performance of the proposed NARX-AWSCKF model and examine its ability to accurately estimate the SOC at different charge-discharge rates, as presented in Fig. 7.

Fig. 7 presents the critical performance evaluation of the optimized NARX network and proposed NARX-AWSCKF model at different charge-discharge rates under the BBDST, DST, and HPPC working conditions using the MAE, RMSE, and MAPE metrics. Under the BBDST working condition, at low- and high-power rates, it can be observed that the optimized NARX network has overall best MAE, RMSE, and MAPE values of 0.1606%, 0.5166%, and 1.6263%, respectively. Meanwhile, the proposed NARX-AWSCKF model has overall best MAE, RMSE, and MAPE values of 0.0623%, 0.1259%, and 1.2477%, respectively, which represent a performance improvement of 61.21%, 75.63%, and 23.28%. Under the DST working condition, it can also be observed that theoptimized NARX network has overall best MAE, RMSE, and MAPE values of 0.3138%, 0.4814%, and 1.0468%, respectively. Meanwhile, the proposed NARX-AWSCKF model has the overall best MAE, RMSE, and MAPE values of 0.2554%, 0.2972%, and 0.4036%, representing performance improvement values of 18.61%, 38.26%, and 61.44% at different charge-discharge rates.

Finally, under the HPPC working condition, the optimized NARX network has overall best MAE, RMSE, and MAPE values of 0.4026%, 0.6476%, and 1.6929%, respectively. Meanwhile, the proposed NARX- AWSCKF model has the overall best MAE, RMSE, and MAPE values of 0.2238%, 0.1376%, and 1.0727%, respectively. These metric results represent a performance improvement of 44.41%, 78.75%, and 36.64%, respectively, significantly improving the SOC estimation accuracy and performance for practical BMS applications at different charge-discharge rates.

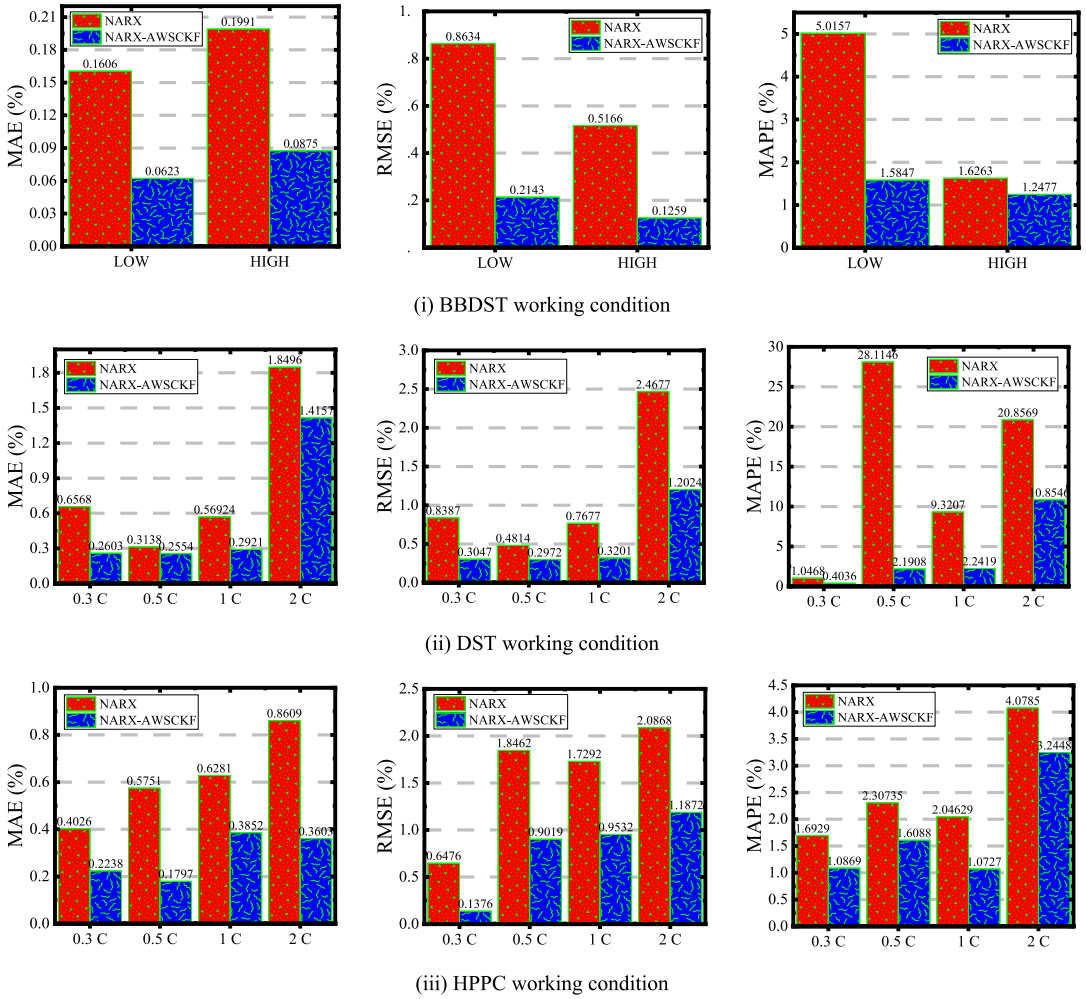

Fig. 7. Performance evaluation of the NARX and NARX-AWSCKF models at different charge-discharge rates under the BBDST, DST, and HPPC working conditions.

4.1.3. SOC estimation at different operating temperatures

The comparative SOC performance results of the NARX and NARX- AWSCKF models are conducted at operating temperatures of O and 45 °C under the BBDST, FUDS, and US06 working conditions. The SOC estimation results at different temperatures under the BBDST working condition are presented in Fig. 8.

In Fig. 8, it can be observed that the SOCs estimated by the NARX network are more stable until close to the end of discharge, where high noise effects and fluctuations are exhibited. At O and 45 °c, the NARX network estimates the SOC with ME values of 1.878% and 2.489%, respectively. Meanwhile, after opt1m1zation, the proposed NARX- AWSCKF model has ME values of 0.2925% and 1.206% at temperatures of O and 45 °C, respectively, with reduced noise and fluctuations, especially at low discharge levels. Furthermore, these results represent a significant performance improvement of 84.42% and 51.55%, respectively.

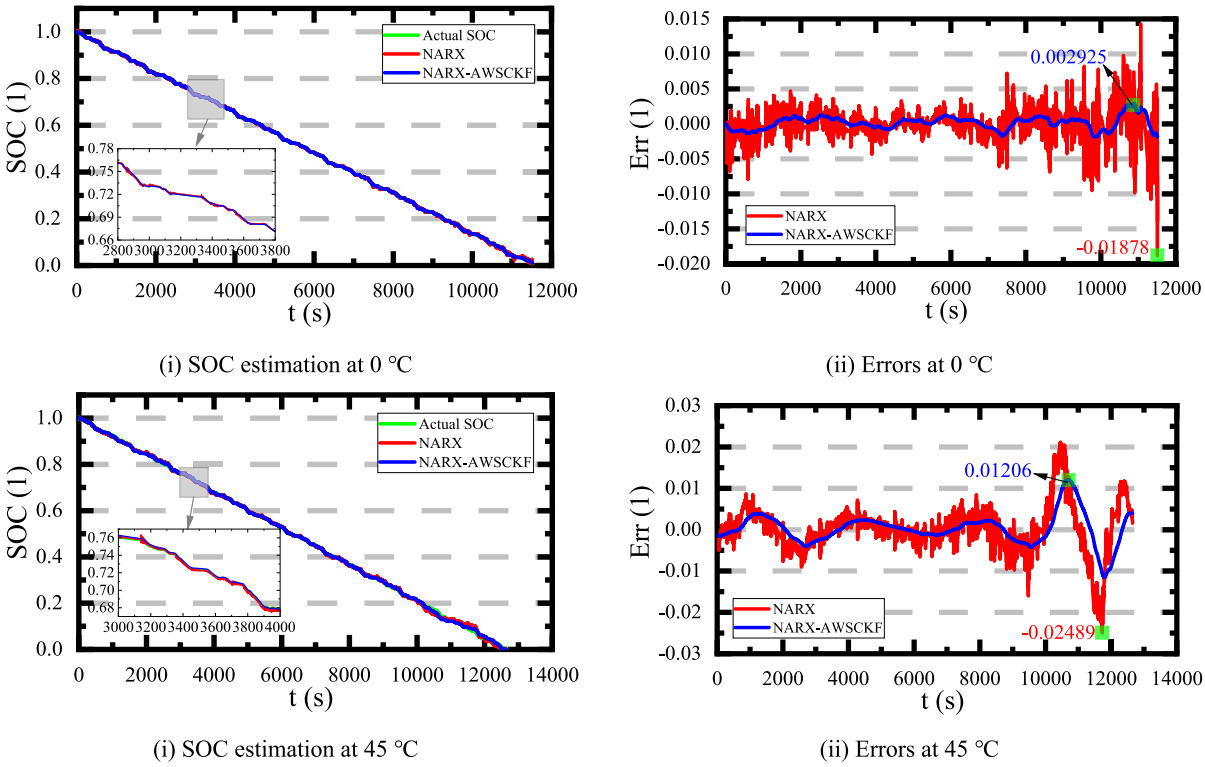

(i) SOC estimation at 0 °C (ii) Errors at 0 °C

(i) SOC estimation at 45 °C (ii) Errors at 45 °C

Fig. 8. Comparative SOC estimation results of the NARX and NARX-AWSCKF models at different temperatures under the BBDST working condition.

Additionally, the comparative SOC performance results of the NARX and NARX-AWSCKF models at 0 and 45 °C under the FUDS working condition are presented in Fig. 9.

Fig. 9 shows the SOC estimation results for the NARX and NARX- AWSCKF models. It can be observed that the NARX network has noise and fluctuations similar to the estimations under the BBDST working condition, especially at 45 °C. However, the results show that the NARX network estimates the SOC with ME values of 2.726% and 2.319% at temperatures of 0 and 45 °C, respectively. Meanwhile, the ME values of the proposed NARX-AWSCKF model are 1.299% and 1.219% for 0 and 45 °C, respectively, which represent a performance improvement of 52.35% and 47.43% after optimization with reduced noise.

Additionally, the comparative SOC performance results of the NARX and NARX-AWSCKF models at 0 and 45 °C under the US06 working condition are presented in Fig. 10.

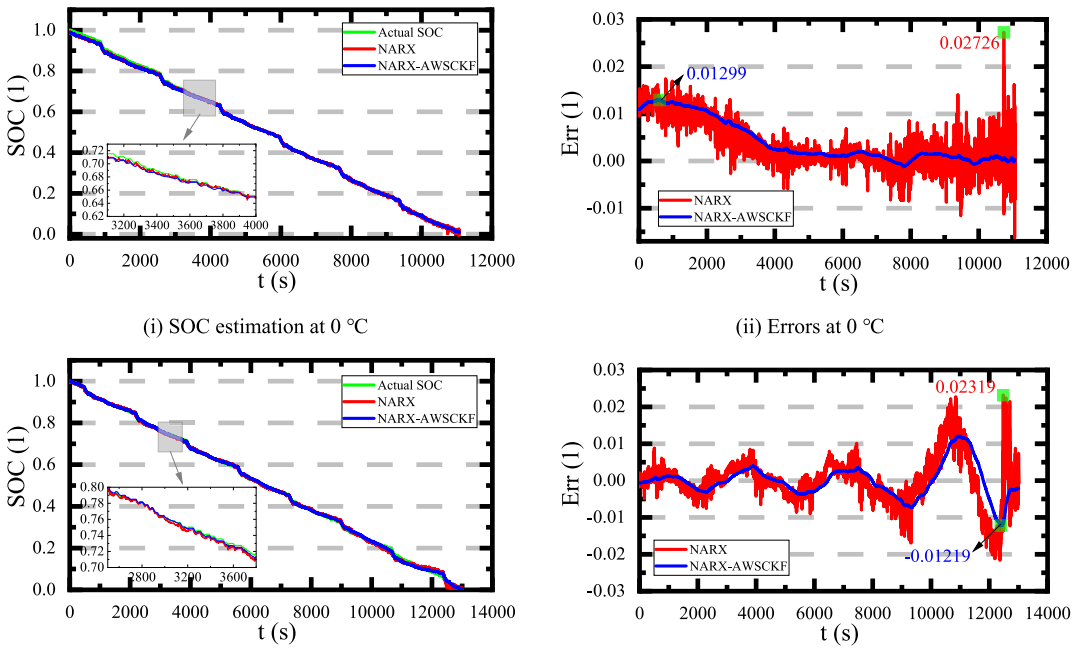

(i) SOC estimation at 0 °C (ii) Errors at 0 °C

(i) SOC estimation at 45 °C (ii) Errors at 45 °C

Fig. 9. Comparative SOC estimation results of the NARX and NARX-AWSCKF models at different temperatures under the FUDS working condition.

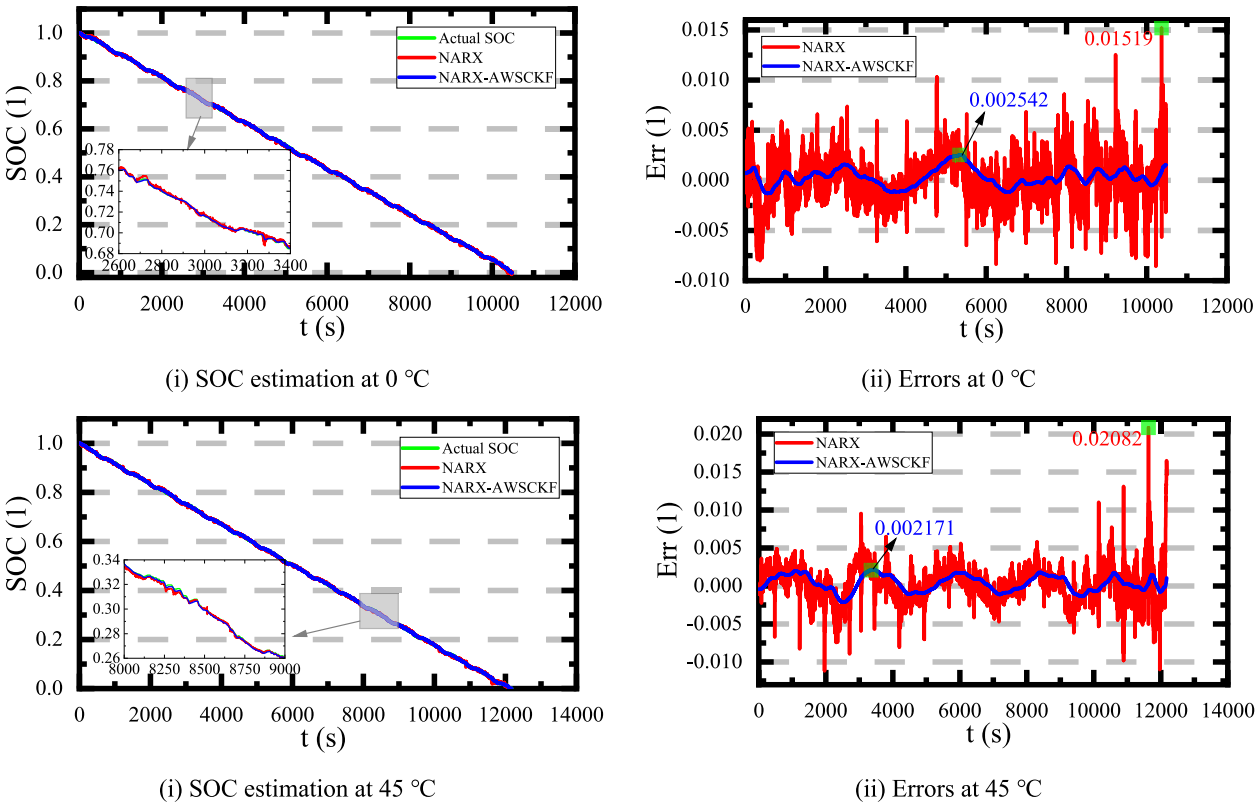

(i) SOC estimation at 0 °C (ii) Errors at 0 °C

(i) SOC estimation at 45 °C (ii) Errors at 45 °C

Fig. 10. Comparative SOC estimation results of the NARX and NARX-AWSCKF models at different temperatures under the US06 working condition.

As presented in Fig. 10, it can be observed that the NARX network exhibits higher noise effects at a temperature of 0°C than at 45°c. It estimates the SOC with ME values of 1.519% and 2.082%, respectively. Meanwhile, at temperatures of 0 and 45 °C, the ME values for the proposed NARX-AWSCKF model are 0.2542% and 0.2171%, signifying a performance improvement of 83.27% and 89.57%, respectively, with highly reduced noise and fluctuations.

Generally, it can be observed that the optimization of the final SOC achieved by the proposed NARX-AWSCKF model has similar characteristics under the BBDST, FUDS, and US06 working conditions, which are consistent and optimally augmented to correct the output of the NARX network to enhance SOC estimation at different operating temperatures for practical BMS applications.

4.1.4. Performance evaluation at different operating temperatures

The critical SOC performance evaluations of the NARX and NARX-AWSCKF models at temperatures of 0 and 45 °C under the BBDST, FUDS, and US06 working conditions are presented in Fig. 11.

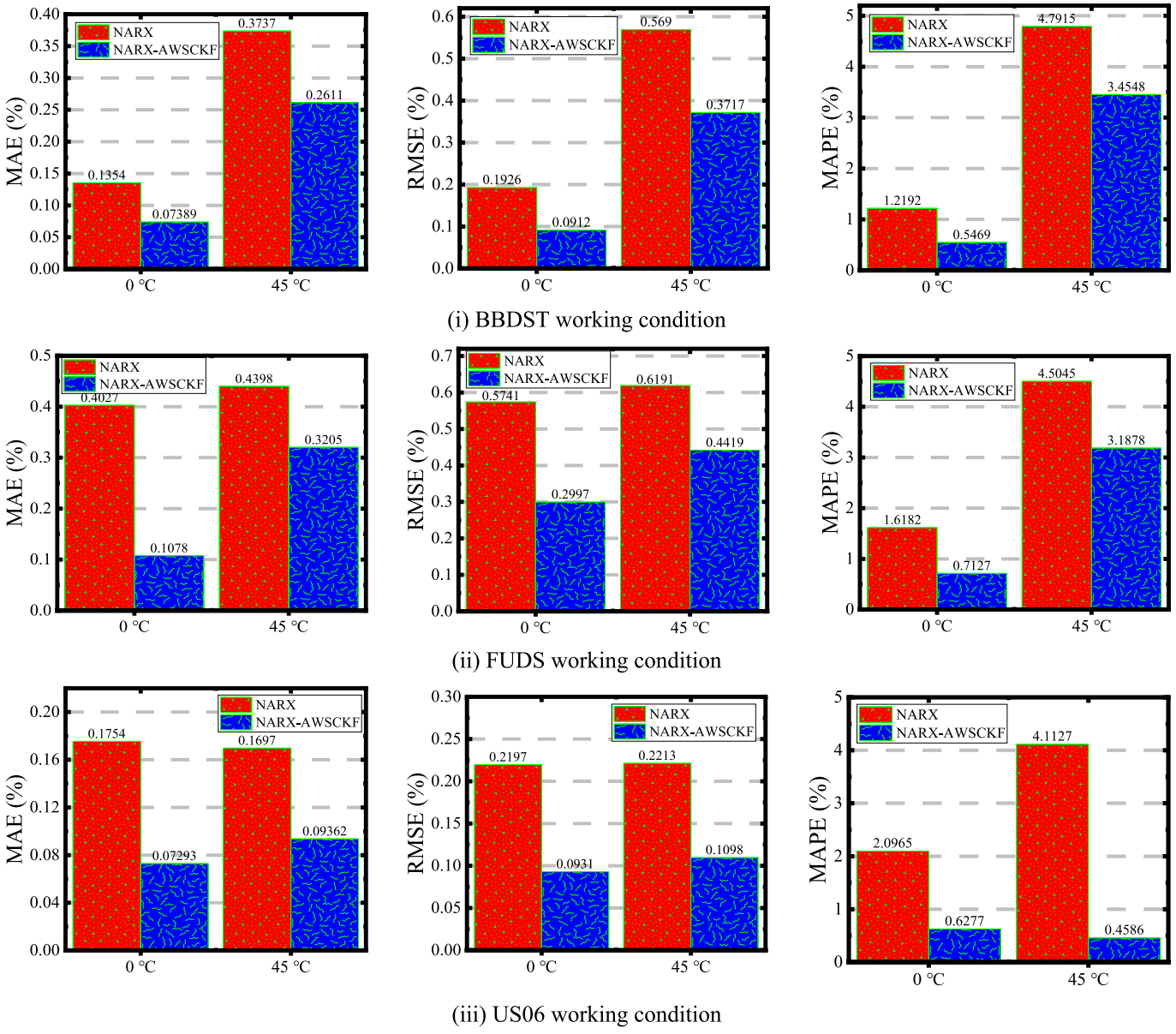

Fig. 11. Performance evaluation of the NARX and NARX-AWSCKF models at different temperatures under the BBDST, FUDS, and US06 working conditions.

In Fig. 11, it can be observed that using the MAE, RMSE, and MAPE metrics, the optimized NARX network has higher error values compared to the proposed NARX-AWSCKF model at different temperatures under the BBDST, FUDS, and US06 working conditions. Under the BBDST working condition, the NARX network estimates the SOC with overall best MAE, RMSE, and MAPE values of0.1354%, 0.1926%, and 1.2192%, respectively. Meanwhile, the proposed NARX-AWSCKF model has 0.07389%, 0.0912%, and 0.5469%, significantly representing a perfor- mance improvement of 45.43%, 52.65%, and 55.14%, respectively.

Under the FUDS working condition, the optimized NARX network has the best overall MAE, RMSE, and MAPE values, with values of 0.4027%, 0.5741%, and 1.6182%, respectively. The proposed NARX- AWSCKF model, however, has the best MAE, RMSE, and MAPE values overall, measuring 0.1078%, 0.2997%, and 0.7127%, respectively. These values correspond significantly to performance improvements of 73.23%, 47.80%, and 44.04% at operating temperatures of O °C and 45 °C.

Finally, at different operating temperatures, the optimized NARX network has the best overall MAE, RMSE, and MAPE values under the US06 working conditions, with values of 0.1697%, 0.2197%, and 2.0965%, respectively. The best MAE, RMSE, and MAPE values are 0.07293%, 0.0931%, and 0.6277%, respectively, for the proposed NARX-AWSCKF model. Using these metric values, they show perfor- mance improvements of 57.02%, 57.62%, and 70.06%, respectively, for the proposed model's accuracy and robustness for SOC estimation at various operating temperatures under complex working conditions in real-world BMS applications.

Furthermore, it can be observed that the optimization by the AWSCKF method optimizes the estimation accuracy and robustness of the optimized NARX network. By providing a suitable trade-off between computational complexity and accuracy, the NARX-AWSCKF model delivers more accurate estimation performance compared to the opti- mized NARX network. Furthermore, it significantly reduces the time-consuming and labor-intensive process compared to other estimation methods and can be used to estimate the SOC of batteries with different chemistries.

4.2. Critical performance comparison of the NARX-AWSCKF model with other existing SOC methods

In addition, the NARX-AWSCKF model is put through a thorough comparative analysis to show that it is superior to other SOC estimation methods that are currently available, as presented in Table 3.

In Table 3, it can be observed that the proposed hybrid models show higher superiority and robustness when compared with the existing SOC estimation methods. According to the study, the ARUKF method comes close, with MAE and RMSE values of 0.69% and 1.22%, respectively, at RT under the DST and CLTC working conditions. Meanwhile, the proposed NARX-AWSCKF model is tested and verified at different temperatures and charge-discharge rates under various complex working conditions, such as the BBDST, DST, HPPC, FUDS, and US06, using batteries with different chemistries that show much accuracy and robustness for SOC estimation, with the overall best MAE, RMSE, and MAPE values of 0.07293%, 0.0912%, and 0.40356%, respectively.

Table 3
Critical performance review of the proposed NARX-AWSCKF model with other existing SOC estimation methods.

Method	Battery	Verification condition	Specification	Optimal metric value	Training time
SCA-SSA-ELM [39]	LiFP120Ah	Temperatures	25-27 °C	MAE= 1.156%	5761.712 s
		Test condition	Lab. test	RMSE = 0.538%	
				MAPE = 0.887%	
TD-RNN [49]	LiFMgP2.5Ah	Temperature	RT	MAE= 1.48%	
		Test conditions	UDDS, NYCC, & UDDS-NYCC		
LSTM-ACKF [57]	LiFP2.23Ah	Temperatures	10--50 °C	ME= 2.2%	
		Test conditions	FUDS, US06, & UDDS	RMSE = 0.8%	
GRU-TL [63]	LiNMC3Ah	Temperatures	32-50 °C	MAE= 0.853%	435.14 s
		Test conditions	FUDS, US06, & UDDS	RMSE = 1.115%	
IBGRU-UKF [64]	LiNMC3Ah	Temperatures	0-40 °C	MAE= 0.50%	
		Test conditions	US06& UDDS	RMSE = 0.62%	
ARUKF [65]	LiNMC40Ah	Temperature	RT	MAE= 0.69%	225 s
		Test conditions	DST& CLTC	RMSE = 1.22%	
LSTM [66]	LiNMC2.9Ah	Temperatures	0-25 °C	MAE= 0.91%	
		Test conditions	US06, LA92, NN, & UDDS	RMSE = 1.02%	
NARX-AWSCKF (Proposed)	LiC2.55Ah & LiNMC2Ah	Temperatures	-10-50 °C	MAE = 0.07293%	79.634 s
		Charge-discharge rates	High-low power, 0.3, 0.5, 1, & 2 C	RMSE = 0.0912%	
		Test conditions	BBDST, DST, HPPC, FUDS, & US06	MAPE = 0.40356%	

Sine cosine algorithm-salp swarm algorithm-extreme learning machine (SCA-SSA-ELM); Time-delayed recurrent neural network (TD-RNN); Gated recurrent unit with transfer learning (GRU-TL); Improved bidirectional GRU-unscented Kalman filter (IBGRU-UKF); Adaptive robust unscented Kalman filter (ARUKF); China automotive test cycle (CLTC); New York city cycle (NYCC); Neural Network (NN) drive cycle.

5. Conclusion and future work

In this paper, a comparative SOC performance study of an optimized NARX network and a proposed NARX-AWSCKF model and its critical review with other existing SOC estimation methods are presented. The SOC estimation results by the NARX network show high noise and fluctuations with high error values. Therefore, this paper proposes an adaptive weighted method that assigns different weights based on the utility of information at different timescales using a moving sliding window and an adaptive weighing coefficient through square-root and cubature updates to optimize the statistical estimation values of the state estimate, error covariance, and measurement noise covariance matrices. The hybrid method estimation process, based on sensitivity analysis and adaptation to different working conditions, increases the SOC accuracy of lithium-ion batteries at different charge-discharge states and temperatures. The results show that the proposed AWSCKF method is effective and robust in filtering out the noise, stabilizing, and optimizing the final SOC at different C-rates and temperatures under five working conditions using two different battery chemistries. The overall best MAE, RMSE, and MAPE values of the proposed NARX-AWSCKF model are 0.07293%, 0.0912%, and 0.40356%, respectively. Finally, compared to other existing methods, the estimation results show that the proposed NARX-AWSCKF model has high accuracy and superiority, which is effective, reliable, and robust for real-time BMS applications in EVs.

Due to the laboratory conditions and limited time, in our future work, experiments using different C-rates at subzero temperatures and aging tests for higher-capacity batteries will be conducted to further verify the performance of the proposed NARX-AWSCKF model for SOC estimation.

CRediT authorship contribution statement

Paul Takyi-Aninakwa: Methodology, conceptualization, software, writing-original draft, analysis, and data curation; **Shunli Wang:** Supervision and resources; **Hongying Zhang:** Resources and investigation; **Yang Xiao:** Writing; **Carlos Fernandez:** Writing.

Declaration of competing interest

The authors declare no known competing financial interests or personal relationships that influence the work reported in this paper.

Data availability

The authors do not have permission to share data.

Acknowledgment

The work is supported by the National Natural Science Foundation of China (No. 62173281 and 61801407).

References

[l] K. Luo, X. Chen, H. Zheng, Z. Shi, A review of deep learning approach to predicting the state of health and state of charge of lithium-ion batteries, J. Energy Chem. 74 (2022) 049, https://doi.org/10.1016/j.jechem.2022.06.049.

[2] Q. Gong, P. Wang, Z. Cheng, A novel deep neural network model for estimating the state of charge of lithium-ion battery, J. Energy Storage 54 (2022), 105308, https://doi.org/10.1016/j.est.2022.105308.

[3] S. Zhang, X. Zhang, A multi time-scale framework for state-of-charge and capacity estimation of lithium-ion battery under optimal operating temperature range, J. Energy Storage 35 (2021), 102325, https://doi.org/10.1016/j.est.2021.102325.

[4] L. Li, Y. Ren, K. o·Regan, U.R. Koleti, E. Kendrick, W.D. Widanage, J. Marco, Lithium-ion battery cathode and anode potential observer based on reduced-order electrochemical single particle model, J. Energy Storage 44 (2021), 103324, https://doi.org/10.1016/j.est.2021.103324.

[5] J. Chen, X. Feng, L. Jiang, Q. Zhu, State of charge estimation of lithium-ion battery using denoising autoencoder and gated recurrent unit recurrent neural network, Energy 227 (2021), 120451, https://doi.org/10.1016/j.energy.2021.120451.

[6] W. Li, M. Luo, Y. Tan, X. Cui, Online parameters identification and state of charge estimation for lithium-ion battery using adaptive cubature Kalman filter, World Electr. Veh. J. 12 (2021) 123, https://doi.org/10.3390/wevjl2030123.

[7] C. Yang, X. Wang, Q. Fang, H. Dai, Y. Cao, X. Wei, An online SOC and capacity estimation method for aged lithium-ion battery pack considering cell inconsistency, J. Energy Storage 29 (2020), 101250, https://doi.org/10.1016/j. est.2020.101250.

[8] C. Jiang, S. Wang, B. Wu, C. Fernandez, X. Xiong, J. Coffie-Ken, A state-of-charge estimation method of the power lithium-ion battery in complex conditions based on adaptive square root extended Kalman filter, Energy 219 (2021), 119603, https://doi.org/10.1016/j.energy.2020.119603.

[9] P. Takyi-Aninakwa, S. Wang, H. Zhang, E. Appiah, E.D. Bobobee, C. Fernandez, A strong tracking adaptive fading-extended Kalman filter for the state of charge estimation oflithium-ion batteries, Int. J. Energy Res. 46 (2022) 8307, https://doi. org/10.1002/er.8307.

[10] Y. Miao, Z. Gao, Estimation for state of charge of lithium-ion batteries by adaptive fractional-order unscented Kalman filters, J. Energy Storage 51 (2022), 104396, https://doi.org/10.1016/j.est.2022.104396.

[11] P. Takyi-Aninakwa, S. Wang, H. Zhang, Y. Xiao, C. Fernandez, A hybrid probabilistic correction model for the state of charge estimation of lithium-ion batteries considering dynamic currents and temperatures, Energy (2023), 127231, https://doi.org/10.1016/j.energy.2023.127231.

[12] W. Duan, C. Song, S. Peng, F. Xiao, Y. Shao, S. Song, An improved gated recurrent unit network model for state-of-charge estimation of lithium-ion battery, Energies 13 (2020) 6366, https://doi.org/10.3390/enl3236366.

[13] H. Shi, S. Wang, C. Fernandez, C. Yu, W. Xu, E.D. Bobobee, L. Wang, Improved multi-time scale lumped thermoelectric coupling modeling and parameter dispersion evaluation of lithium-ion batteries, Appl. Energy 324 (2022), 119789, https://doi.org/10.1016/j.apenergy.2022.119789.

[14] P. Takyi-Aninakwa, S. Wang, H. Zhang, H. Li, W. Xu, C. Fernandez, An optimized relevant long short-term memory-squared gain extended Kalman filter for the state of charge estimation of lithium-ion batteries, Energy 260 (2022), 125093, https:// doi.org/10.1016/j.energy.2022.125093.

[15] P. Takyi-Aninakwa, S. Wang, H. Zhang, X. Yang, C. Fernandez, An optimized long short-term memory-weighted fading extended Kalman filtering model with wide temperature adaptation for the state of charge estimation of lithium-ion batteries, Appl. Energy 326 (2022), 120043, https://doi.org/10.1016/j.apenergy.2022.120043.

[16] Z. Chen, H. Zhao, X. Shu, Y. Zhang, J. Shen, Y. Liu, Synthetic state of charge estimation for lithium-ion batteries based on long short-term memory network modeling and adaptive H-Infinity filter, Energy 228 (2021), 120630, https://doi. org/10.1016/j.energy.2021.120630.

[17] K. McCarthy, H. Gullapalli, K.M. Ryan, T. Kennedy, Electrochemical impedance correlation analysis for the estimation of Li-ion battery state of charge, state of health and internal temperature, J. Energy Storage 50 (2022), 104608, https://doi. org/10.1016/j.est.2022.l 04608.

[18] Y. Wang, Y. Cheng, Y. Xiong, Q. Yan, Estimation of battery open-circuit voltage and state of charge based on dynamic matrix control - extended Kalman filter algorithm, J. Energy Storage 52 (2022), 104860, https://doi.org/10.1016/j.est.2022.104860.

[19] M. Esser, G. Rohde, C. Rehtanz, Electrochemical impedance spectroscopy setup based on standard measurement equipment, J. Power Sources 544 (2022), 231869, https://doi.org/10.1016/j.jpowsour.2022.231869.

[20] M.A. Hannan, M.S.H. Lipu, A. Hussain, A. Mohamed, A review of lithium-ion battery state of charge estimation and management system in electric vehicle applications: challenges and recommendations, Renew. Sust. Energ. Rev. 78 (2017) 834-854, https://doi.org/10.1016/j.rser.2017.05.001.

[21] P. Yu, S. Wang, C. Yu, W. Shi, B. Li, Study of hysteresis voltage state dependence in lithium-ion battery and a novel asymmetric hysteresis modeling, J. Energy Storage 51 (2022), 104492, https://doi.org/10.1016/j.est.2022.104492.

[22] Y. Gao, G.L. Plett, G. Fan, X. Zhang, Enhanced state-of-charge estimation of LiFePO4 batteries using an augmented physics-based model, J. Power Sources 544 (2022), 231889, https://doi.org/10.1016/j.jpowsour.2022.231889.

[23] H. Pan, Z. Lii, W. Lin, J. Li, L. Chen, State of charge estimation of lithium-ion batteries using a grey extended Kalman filter and a novel open-circuit voltage model, Energy 138 (2017) 764-775, https://doi.org/10.1016/j.energy.2017.07.099.

[24] U.N. Jibhkate, U.B. Mujumdar, Development of low complexity open circuit voltage model for state of charge estimation with novel curve modification technique, Electrochim. Acta 429 (2022), 140944, https://doi.org/10.1016/j. electacta.2022.140944.

[25] **J.** Hong, Z. Wang, W. Chen, **L.-Y.** Wang, C. Qu, Online joint-prediction of multi- forward-step battery SOC using **LSTM** neural networks and multiple linear regression for real-world electric vehicles, **J.** Energy Storage 30 (2020), 101459, https://doi.org/10.1016/j.est.2020.101459.

[26] W. Ma, P. Guo, X. Wang, Z. Zhang, S. Peng, B. Chen, Robust state of charge estimation for Li-ion batteries based on cubature Kalman filter with generalized maximum correntropy criterion, Energy 260 (2022), 125083, https://doi.org/ 10.1016/j.energy.2022.125083.

[27] M.A. Hannan, S.B. Wali, P.J. Ker, M.S. Abd Rahman, M. Mansor, V. K. Ramachandaramurthy, K.M. Muttaqi, T.M.I. Mahlia, Z.Y. Dong, Battery energy- **storage system: a review of technologies, optimization objectives, constraints,** approaches, and outstanding issues, J. Energy Storage 42 (2021) 103023, https:// doi.org/10.1016/j.est.2021.l 03023.

[28] L. Ling, D. Sun, X. Yu, R. Huang, State of charge estimation of Lithium-ion batteries based on the probabilistic fusion of two kinds of cubature Kalman filters, J. Energy Storage 43 (2021), 103070, https://doi.org/10.1016/j.est.2021.103070.

[29] H. Shi, S. Wang, J. Liang, P. Takyi-Aninakwa, X. Yang, C. Fernandez, L. Wang, Multi-time scale identification of key kinetic processes for lithium-ion batteries considering variable characteristic frequency, J. Energy Chem. 022 (2023), https:// doi.org/10.1016/j.jechem.2023.02.022.

[30] Y. Ye, Z. Li, J. Lin, X. Wang, State-of-charge estimation with adaptive extended Kalman filter and extended stochastic gradient algorithm for lithium-ion batteries, **J.** Energy Storage 47 (2022), 103611, https://doi.org/10.1016/j.est.2021.103611.

[31] Z. Chen, J. Zhou, F. Zhou, S. Xu, State-of-charge estimation of lithium-ion batteries based on improved **H** infinity filter algorithm and its novel equalization method, **J.** Clean. Prod. 290 (2021), 125180, https://doi.org/10.1016/j.jclepro.2020.125180.

[32] Z. Cui, W. Hua, G. Zhang, Z. Zhang, Z. Chen, An extended Kalman filter based SOC estimation method for Li-ion battery, Energy Rep. 8 (2022) 81-87, https://doi.org/ 10.1016/j.egyr.2022.02.116.

[33] L. Chen, X. Wu, A.M. Lopes, L. Yin, P. Li, Adaptive state-of-charge estimation of lithium-ion batteries based on square-root unscented Kalman filter, Energy 252 (2022), 123972, https://doi.org/10.10l 6/j.energy.2022.123972.

[34] Y. Wang, Z. Chen, A framework for state-of-charge and remaining discharge time prediction using unscented particle filter, Appl. Energy 260 (2020), 114324, https://doi.org/10.1016/j.apenergy.2019.114324.

[35] I. Oyewole, A. Chehade, Y. Kim, A controllable deep transfer learning network with multiple domain adaptation for battery state-of-charge estimation, Appl. Energy 312 (2022), 118726, https://doi.org/10.1016/j.apenergy.2022.118726.

[36] Y. Li, K. Li, X. Liu, X. Li, L. Zhang, B. Renie, T. Sun, K.T.V. Grattan, A hybrid machine learning framework for joint SOC and SOH estimation of lithium-ion batteries assisted with fiber sensor measurements, Appl. Energy 325 (2022), 119787, https://doi.org/10.1016/j.apenergy.2022.119787.

[37] S. Li, H. He, C. Su, P. Zhao, Data driven battery modeling and management method with aging phenomenon considered, Appl. Energy 275 (2020), 115340, https://doi.org/10.1016/j.apenergy.2020.115340.

[38] Y. Song, D. Liu, H. Liao, Y. Peng, A hybrid statistical data-driven method for on-line joint state estimation of lithium-ion batteries, Appl. Energy 261 (2020), 114408, https://doi.org/10.1016/j.apenergy.2019.114408.
[39] J. Dou, H. Ma, Y. Zhang, S. Wang, Y. Ye, S. Li, L. Hu, Extreme learning machine model for state-of-charge estimation of lithium-ion battery using salp swarm algorithm, J. Energy Storage 52 (2022), 104996, https://doi.org/10.1016/j.est.2022.104996.
[40] K. Yang, Y. Tang, S. Zhang, Z. Zhang, A deep learning approach to state of charge **estimation of lithium-ion batteries based on dual-stage attention mechanism,** Energy 244 (2022), 123233, https://doi.org/10.1016/j.energy.2022.123233.
[41] J. Tian, R. Xiong, W. Shen, J. Lu, State-of-charge estimation of $LiFePO_4$ batteries in electric vehicles: a deep-learning enabled approach, Appl. Energy 291 (2021), 116812, https://doi.org/10.1016/j.apenergy.2021.116812.
[42] X. Wu, M. Li, J. Du, F. Hu, SOC prediction method based on battery pack aging and consistency deviation of thermoelectric characteristics, Energy Rep. 8 (2022) 2262-2272, https://doi.org/10.1016/j.egyr.2022.01.056.
[43] Q. Wang, H. Gu, M. Ye, M. Wei, X. Xu, State of charge estimation for lithium-ion battery based on NARX recurrent neural network and moving window method, IEEE Access 9 (2021) 83364-83375, https://doi.org/10.1109/ACCESS.2021.3086507.
[44] A. Herle, J. Channegowda, K. Naraharisetti, Analysis of NARXNN for state of charge estimation for Ii-ion batteries on various drive cycles, in: 2020 8th International Conference on Power Electronics Systems and Applications (PESA), 2020, pp. 1-4, https://doi.org/l0.48550/arXiv.2012.10725.
[45] G. Chuangxin, Y. Gen, C. Zhu, X. Wang, X. Cao, Soc estimation for lithium-ion battery using recurrent NARX neural network and genetic algorithm, in: !OP Conference Series: Materials Science and Engineering 486, 2019, 012076, https:// doi.org/10.1088/l757-899X/486/1/012076.
[46] G. Abbas, M. Nawaz, F. Kamran, Performance comparison of NARX & RNN-LSTM neural networks for $LiFePO_4$ battery state of charge estimation, in: 2019 16th International Bhurban Conference on Applied Sciences and Technology (IBCAST), Islamabad, Pakistan, 2019, pp. 463-468, https://doi.org/10.1109/IBCAST.2019.8667172.
[47] M. Wei, M. Ye, J.B. Li, Q. Wang, X. Xu, State of charge estimation of lithium-ion batteries using LSTM and NARX neural networks, IEEE Access 8 (2020) 189236--189245, https://doi.org/10.1109/ACCESS.2020.3031340.
[48] X. Ren, S. Liu, X. Yu, X. Dong, A method for state-of-charge estimation of lithium- ion batteries based on PSO-LSTM, Energy 234 (2021), 121236, https://doi.org/ 10.1016/j.energy.2021.121236.
[49] Z. Xi, R. Wang, Y. Fu, C. Mi, Accurate and reliable state of charge estimation of lithium ion batteries using time-delayed recurrent neural networks through the identification of overexcited neurons, Appl. Energy 305 (2022), 117962, https:// doi.org/10.1016/j.apenergy.2021.117962.
[50] C. Bian, H. He, S. Yang, Stacked bidirectional long short-term memory networks for state-of-charge estimation of lithium-ion batteries, Energy 191 (2020), 116538, https://doi.org/10.1016/j.energy.2019.116538.
[51] M. Fasahat, M. Manthouri, State of charge estimation of lithium-ion batteries using hybrid autoencoder and long short term memory neural networks, J. Power Sources 469 (2020), 228375, https://doi.org/10.1016/j.jpowsour.2020.228375.
[52] F. Yang, S. Zhang, W. Li, Q. Miao, State-of-charge estimation of lithium-ion batteries using LSTM and UKF, Energy 201 (2020), 117664, https://doi.org/ 10.1016/j.energy.2020.117664.
[53] J. Chen, Y. Zhang, W. Li, W. Cheng, Q. Zhu, State of charge estimation for lithium- **ion batteries using gated recurrent unit recurrent neural network and adaptive** Kalman filter, J. Energy Storage 55 (2022), 105396, https://doi.org/10.1016/j. est.2022.105396.
[54] H. Zuo, B. Zhang, Z. Huang, K. Wei, H. Zhu, J. Tan, Effect analysis on SOC values of the power lithium manganate battery during discharging process and its intelligent estimation, Energy 238 (2022), 121854, https://doi.org/10.1016/j.energy.2021.121854.
[55] M.S.H. Lipu, M.A. Hannan, A. Hussain, M.H.M. Saad, A. Ayob, F. Blaabjerg, State of **charge estimation for lithium-ion battery using recurrent NARX neural network** model based lighting search algorithm, IEEE Access 6 (2018) 28150-28161, https://doi.org/10.1109/ACCESS.2018.2837156.
[56] Y. Liu, J. Wang, Transfer learning based multi-layer extreme learning machine for probabilistic wind power forecasting, Appl. Energy 312 (2022), 118729, https://doi.org/10.1016/j.apenergy.2022.118729.
[57] Y. Tian, R. Lai, X. Li, L. Xiang, J. Tian, A combined method for state-of-charge estimation for lithium-ion batteries using a long short-term memory network and an adaptive cubature Kalman filter, Appl. Energy 265 (2020), 114789, https://doi. org/10.1016/j.apenergy.2020.114789.
[58] P. Takyi-Aninakwa, S. Wang, H. Zhang, Y. Xiao, C. Fernandez, Enhanced multi- **state estimation methods for lithium-ion batteries considering temperature** uncertainties, J. Energy Storage 66 (2023) 107495. https://doi.org/10.1016/j.est. 2023.107495.
[59] X. Li, Z. Huang, J. Tian, Y. Tian, State-of-charge estimation tolerant of battery aging based on a physics-based model and an adaptive cubature Kalman filter, Energy 220 (2021), 119767, https://doi.org/10.1016/j.energy.2021.119767.
[60] W. Liu, T. Placke, K.T. Chau, Overview of batteries and battery management for electric vehicles, Energy Rep. 8 (2022) 4058-4084, https://doi.org/10.1016/j.egyr.2022.03.016.
[61] L.A. Roman-Ramirez, J. Marco, Design of experiments applied to lithium-ion batteries: a literature review, Appl. Energy 320 (2022), 119305, https://doi.org/ 10.1016/j.apenergy.2022.119305.
[62] R. Xiao, Y. Hu, X. Jia, G. Chen, A novel estimation of state of charge for the lithium- ion battery in electric vehicle without open circuit voltage experiment, Energy 243 (2022), 123072, https://doi.org/10.1016/j.energy.2021.123072.
[63] Y.-X. Wang, Z. Chen, W. Zhang, Lithium-ion battery state-of-charge estimation for small target sample sets using the improved GRU-based transfer learning, Energy 244 (2022), 123178, https://doi.org/10.1016/j.energy.2022.123178.
[64] Z. Cui, L. Kang, L. Li, L. Wang, K. Wang, A combined state-of-charge estimation method for lithium-ion battery using an improved BGRU network and UKF, Energy 259 (2022), 124933, https://doi.org/10.1016/j.energy.2022.124933.
[65] L. Wang, J. Ma, X. Zhao, X. Li, K. Zhang, Z. Jiao, Adaptive robust unscented Kalman filter-based state-of-charge estimation for lithium-ion batteries with multi- parameter updating, Electrochim. Acta 426 (2022), 140760, https://doi.org/ 10.1016/j.electacta. 2022.140760.
[66] L. Ma, C. Hu, F. Cheng, State of charge and state of energy estimation for lithium- ion batteries based on a long short-term memory neural network, J. Energy Storage 37 (2021), 102440, https://doi.org/10.1016/j.est.2021.102440.